A High-Efficiency System for Long-Term Salinity-Gradient Energy Harvesting and Simultaneous Solar Steam Generation

Jun Long, Jun Yin, Fuhua Yang, Guangmin Zhou, Hui-Ming Cheng, Wanlin Guo,* and Ling Qiu**

The vast energy stored in the ocean, which receives an average solar power of ≈60 000 TW per year, surpasses human energy consumption by three orders of magnitude. Harnessing even a small fraction of it holds great promise in addressing global energy and water crises. Here, an integrated device that achieves unprecedented power density up to 1.1 W m^{-2} with excellent stability through a salinity concentration gradient induced by solar evaporation, while simultaneously producing clean water at a rate of 1.25 kg m^{-2} h^{-1} under one sun irradiation is presented. The remarkable electricity generation capability stems from the unique interlayer structure of polyaniline-graphene oxide-MnO_2 (PANI@GO/MnO_2) electrodes, enabling the recovery of electrochemical potentials from a wide range of ion salinity concentrations within the device and the additional Donnan potential generated by the anion-exchange membrane. Furthermore, periodic flipping of the device effectively reactivates the electrodes and suppresses salt accumulation, enabling long-term operation. Notably, a prototype device of 8 × 25 cm^2 exhibits a short-circuit current of 10 mA and an open-circuit voltage of 10.2 V, as well as a clean water production rate of 24.8 g per hour. These findings shed light on the reliable technology for power and freshwater supply in marine environments.

1. Introduction

Renewable energy and access to clean water are essential for sustaining human daily life.[1–3] However, these resources are often scarce, particularly in remote off-grid areas characterized by geographical isolation, especially in developing countries.[4,5] The ocean receives an average power ≈60 000 TW from the sun, which can compensate for one-third of global energy consumption on the condition that a 1% efficiency can be achieved in harnessing 1% of the energy from solar steam generation. Unfortunately, the effective utilization of this energy remains limited due to the lack of efficient methods.[1] The pursuit of harnessing blue energy from water sources has long been recognized as a pressing need.[6] In previous studies, various approaches have been applied to produce electricity from the abundant energy in oceans, which are mainly based on membrane technologies,[7–10] pressure retarded osmosis,[11–15] and electrochemical devices (including reverse electrodialysis and capacitive mixing).[16,17] However, these techniques are largely confined to river-sea junctions, necessitate expensive equipment, and often involve the consumption of freshwater resources.

Recently, significant advancements have been made in the development of advanced integrated devices capable of harvesting

J. Long, G. Zhou, L. Qiu
Shenzhen Geim Graphene Center
Tsinghua-Berkeley Shenzhen Institute & Tsinghua Shenzhen International Graduate School
Tsinghua University
Shenzhen 518055, China
E-mail: ling.qiu@sz.tsinghua.edu.cn

J. Long, W. Guo
College of Materials Science and Engineering
Shenzhen University
Shenzhen 518055, China
E-mail: wlguo@nuaa.edu.cn

J. Yin
Key Laboratory for Intelligent Nano Materials and Devices of Ministry of Education
State Key Laboratory of Mechanics and Control of Mechanical Structures
Nanjing University of Aeronautics and Astronautics
Nanjing 210016, China
E-mail: yinjun@nuaa.edu.cn

F. Yang
Helmholtz Institute Ulm
Helmholtzstrasse 11, D-89081 Ulm, Germany

H.-M. Cheng
Faculty of Materials Science and Energy Engineering
Institute of Technology for Carbon Neutrality
Shenzhen Institute of Advanced Technology
Chinese Academy of Sciences
Shenzhen 518055, China

energy in locations where both sunlight and ocean water are readily available. These innovative devices have significantly expanded the potential application areas. Notably, these integrated devices can effectively harness different forms of energy in the interfacial solar steam generation process.[18–21] For instance, Zhu's group demonstrated the simultaneous generation of electricity and clean water through an integrated system that stores and recycles steam enthalpy using a commercial thermoelectric module within the interfacial solar steam generation process.[22]

From a practical perspective, the design of devices for energy recovery and freshwater production through interfacial solar steam generation faces several systemic challenges that need to be addressed before achieving practical applications. 1) The system should be sustainable. Traditional electrochemistry-based devices, for instance, osmotic energy harvesters, rely on ion-electron exchange at the liquid-electrode interface. Thus, reversible electrodes, such as Ag/AgCl, are required. However, their consumption would lead to a limited working time for the device. Novel electrode design and working strategy are required for harvesting the salinity-gradient energy sustainably. 2) Unlike in river-sea junctions where the salt concentration difference remains relatively constant, the salinity generated during the solar evaporation process exhibits a wide range, varying from 0.2 to 6.0 mol L^{-1}. Most reported aqueous power-generating devices are designed to operate within specific salt concentration ranges. Overcoming this challenge requires innovative electrode and device designs that can accommodate and maintain high energy recovery efficiency under varying salinity conditions. 3) The salt crystal precipitation can impede the water-evaporation and potentially damage the device, leading to reduced performance.[23,24] Effective strategies must be developed to mitigate salt crystal precipitation within the device, ensuring continuous and efficient operation. 4) The integrated device should be designed to be cost-effective, simple, and exhibit long-term stability while achieving high energy conversion efficiency. These additional requirements pose further challenges in terms of device architecture, material selection and manufacturing processes.

In this study, we have developed an integrated system capable of spontaneously generating electricity and fresh water over an extended period through utilizing the osmotic energy induced by solar evaporation. The system employs interlayer structure of polyaniline-graphene oxide-MnO_2 (PANI@GO/MnO_2)electrodes and an anion-exchange membrane (AEM) to leverage the combined effects of Donnan potentials and electrochemical potentials. Through the evaporation of seawater under one sun, a salinity gradient is created, enabling the system to achieve a remarkable maximum power density of ≈1.1 W m^{-2}. Experimental results demonstrate the system's high performance, with a short-circuit current (I_{sc}) of 72.5 mA and an open-circuit voltage (V_{oc}) of 0.31 V achieved using a 100 cm^2 integrated device under one sun irradiation. Notably, the symmetrical electrodes comprising PANI@GO/MnO_2, with a large interlayer distance, exhibit excellent stability and reversibility across a wide range of NaCl concentrations, spanning from 0.2-6.0 mol L^{-1}. To prevent the crystallization and accumulation of salt on the surface of the solar absorber, periodic flipping of the integrated device effectively suppresses these phenomena. During the operation of the system, it autonomously produces drinkable water at a rate of 1.25 kg m^{-2} h^{-1}. Moreover, the device demonstrates continuous operation for a duration of 240 h, highlighting its long-term stability and reliability.

2. Results and Discussion

The integrated device designed for simultaneous electricity and clean water generation is displayed in **Figure 1a**. One of the key features of the device is its ability to effectively suppress the crystallization and accumulation of salt through periodic flipping. The device incorporates a hybrid electrode structure comprising a layer of solar absorbers, current collectors, and PANI@GO/MnO_2 electrodes (Figure 1b). The PANI@GO/MnO_2 was synthesized via an inorganic/organic interfacial reaction and subsequently coated onto carbon cloth. Further details regarding the fabrication method and structural characterization can be found (in the Experimental Section and Figures S1–S3, Supporting Information). The typical scanning electron microscopy (SEM) image of the hybrid electrode cross-section is presented in Figure S4 (Supporting Information), elucidating the interlayer structure of the hybrid electrode. And the SEM confirmed the morphology of the PANI@GO/MnO_2, revealing flake-like debris (Figure 1c). The inset in Figure 1c displays a high-resolution transmission electron microscope (HR-TEM) image of PANI@GO/MnO_2, highlighting the expanded interlayer spacing of ≈1.2 nm.

Additionally, the Mn 3s doublet spectra displayed a spin-energy separation of 4.76 eV in the PANI@GO/MnO_2 (Figure 1d), demonstrating ≈4.0 charge state of Mn.[25] The PANI@GO/MnO_2 with Mn^{4+}-rich phases provides a greater number of active sites, enhancing the stability of the crystal structure during electric power generation. The binding energy of C1s spectra for adventitious carbon is commonly acknowledged to be at 284.80 eV. Pure MnO_2 was chosen as the sample without containing carbon for analysis and calibration of the charging effect (in Figure S5, Supporting Information). The light absorber component of the device facilitates the concentration of heat during solar irradiation, leading to the generation of vapor, which subsequently condenses to form water and flows along the water channel on the container wall (Figure. 1a). Simultaneously, a salinity gradient was generated between the two sides of the AEM, resulting in a notable potential developed between two symmetrical PANI@GO/MnO_2 electrodes. The power density of the device is calculated by dividing the produced power by the effective membrane area, typically measured as 1 cm × 1 cm, unless otherwise stated.

In our study, we utilized pre-acidized multi-walled carbon nanotubes (MWCNTs) and graphite as the light absorber materials due to their efficient absorption capabilities and excellent stability. The light absorber materials were dropcasted onto pre-treated carbon cloth, resulting in a flexible black membrane (see details in Experimental Section, Figures S6 and S7, Supporting Information). The MWCNTs and the graphite on the pre-treated carbon

H.-M. Cheng
Shenyang National Laboratory for Materials Science
Institute of Metal Research
Chinese Academy of Sciences
Shenyang 110016, China

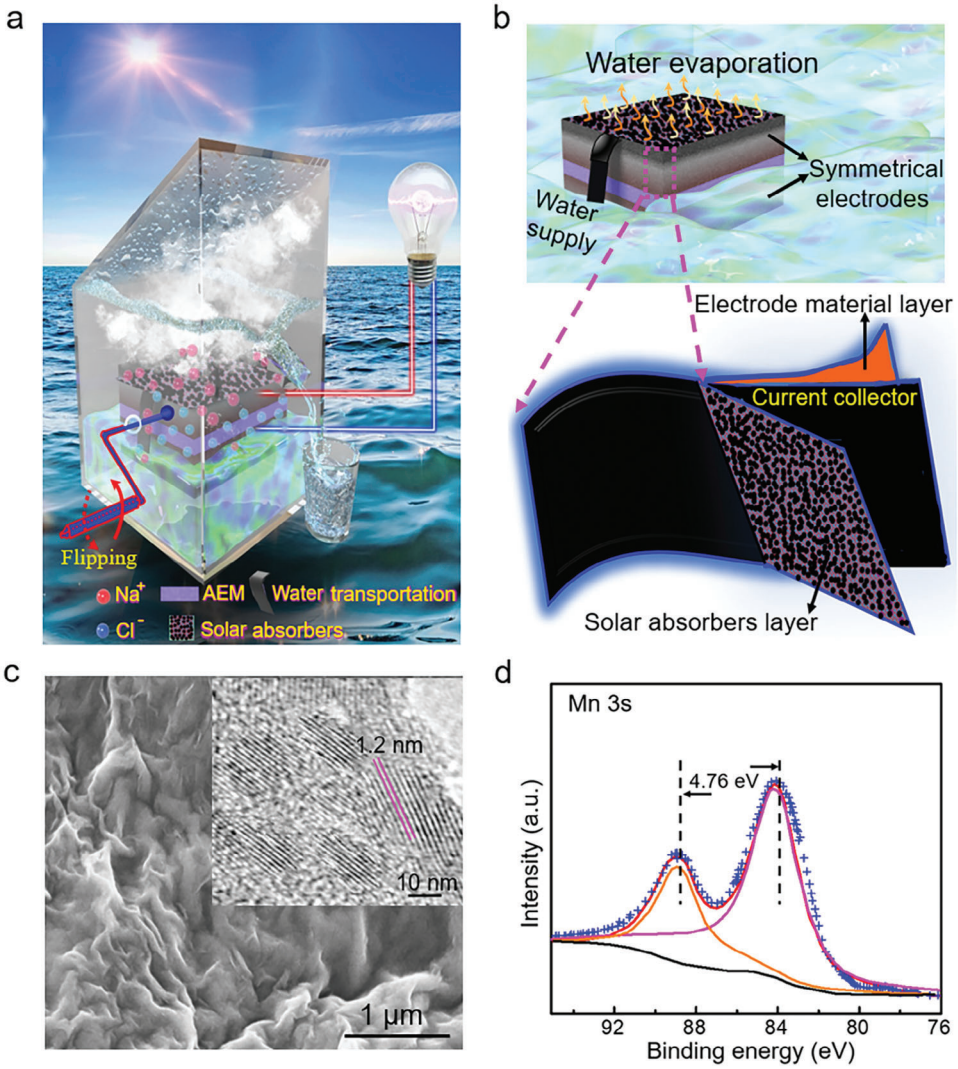

Figure 1. Schematic of the integrated device. a) Schematics of the integrated device for generating electricity and clean water simultaneously from the solar-driven interfacial evaporation process. The device incorporates a flipping design to prevent salt crystal precipitation and activate the electrode. b) The hybrid electrode is composed of a solar absorbers layer, a current collector, and an electrode material layer. c) SEM image of PANI@GO/MnO_2, the inset shows its corresponding HR-TEM. d) XPS of Mn 3s doublet for PANI@GO/MnO_2.

cloth show efficient and broadband absorption (≈95.7% weighted absorption) from 250 to 2500 nm (Figure S8, Supporting Information). We further conducted investigations on the evaporation rates and the solar-to-steam efficiency of the light absorber. The schematic of the experimental setup involved the use of a balance to determine the mass loss of water and a thermocouple to measure the real-time temperature of the water in the solar absorber under various solar irradiation conditions (Figure S9, Supporting Information). The formula ($\eta = mh_{LV}/P$) is used to calculate the solar thermal efficiency (η), where m and h_{LV} are the mass flux and the whole phase-changing enthalpy (including phase-changing enthalpy and sensible heat), and P is the solar power density[26,27] (Equations (S1) and (S2), Supporting Information).

As can be seen in **Figure 2**a, the average evaporation rates are 0.56, 1.25, 1.60, and 2.50 kg m^{-2} h^{-1} under solar irradiations of 0.5, 1.0, 1.5, 2.0 kW m^{-2}, respectively, and the corresponding efficiencies are 72.8%, 78.9%, 71.2%, and 84.3%, respectively. These results demonstrate high thermal efficiency, comparable to previously reported findings.[28,29] The mass change of the water (Figure 2b) presented a nearly linear relationship over time under different solar irradiation conditions, which indicated that the system reached a steady state with much-reduced heat loss during the interfacial heating process. Under 2.0 kW m^{-2} solar irradiation, the surface water temperature near the solar absorber increased to 56 °C within ≈55 min and then stabilized, while the bulk water temperature gradually increased from room temperature to 20.5 °C over the same period and subsequently remained steady at 20.5 °C (Figure S10, Supporting Information). The solar absorber concentrates heat, and the AEM effectively inhibits heat transfer to the bulk water, aligning with findings in existing literature.[30] Therefore, the temperature evolution of the solar absorber indicated that higher irradiation power densities required less time to reach a steady state (Figure S10, Supporting Information). The excellent performance of the evaporation layer can be

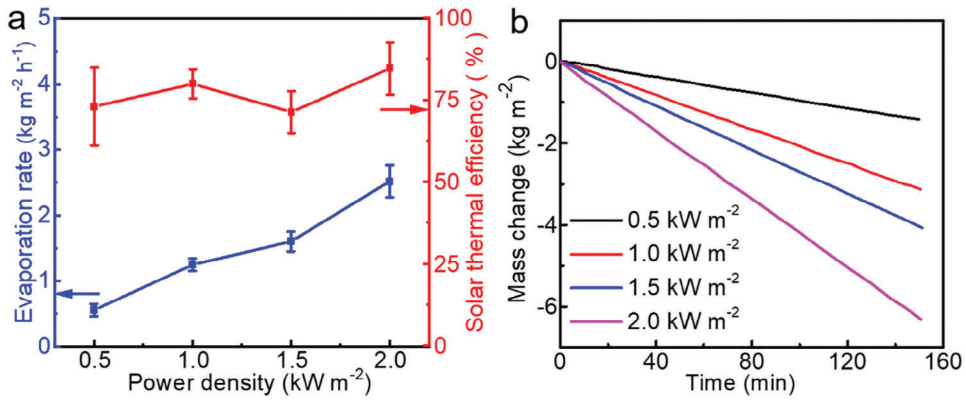

Figure 2. Power production performance of interfacial solar steam generation. a) Evaporation rate and the corresponding solar thermal efficiency under different solar irradiations. b) Mass change of water under different solar irradiations.

attributed to the broadband absorption characteristics of the light absorber layer, as well as the low thermal conductivity of the AEM (0.27–0.32 W m^{-1} k^{-1}). These factors effectively prevent heat loss through the bulk water, contributing to the overall high efficiency of the system.

The NaCl concentration on the top side of the AEM gradually increases as water evaporates from the surface of the solar absorber during the solar steam production process. The NaCl concentration on the top side of the AEM increases from ≈3.6 to 6.0 mol L^{-1} as the solar irradiation power density increases from 0.5 to 2 kW m^{-2} (Figure S11, Supporting Information). The salinity gradient generated between the two sides of the AEM can be used to generate electricity. To evaluate the electricity generation performance of the integrated device, measurements were conducted under varying solar irradiation levels. The V_{oc} increases gradually under solar irradiation until it reaches a steady-state value (**Figure 3a**). As the solar density is increased from 0.5 to 2.0 kW m^{-2}, the steady-state V_{oc} rises from 0.233 to 0.305 V. Figure 3b presents the current-voltage curves of the device under different solar intensities. It can be seen that the I_{sc} of this integrated device reached its maximum (1.52 mA cm^{-2}) at 2.0 kW m^{-2}. The outpower density of the integrated device reaches ≈0.83 and ≈1.22 W m^{-2} at the solar densities of 1.0 and 2.0 kW m^{-2}, respectively (Figure 3c). By optimizing ion diffusion and salinity control through adjustments in the AEM thickness (Figure S12, Supporting Information) and water supplement speed (Figure S13, Supporting Information), the output power of the integrated device can be further enhanced. Specifically, under a solar intensity of 1.0 kW m^{-2}, the output power reaches ≈1.1 W m^{-2}, which is significantly higher than values reported in previous studies focusing on salinity power extraction (refer to Table S1, Supporting Information for comparisons). During the operation of the device, we observed a gradual decrease in the open-circuit voltage (V_{oc}) to 0.03 V after 290 min (Figure 3d). This decrease in V_{oc} was accompanied by the accumulation of salt on the surface of the solar absorber (Figure 3e,f). Salt accumulation is a common issue in devices operating in saline water, as the increasing salt concentration leads to crystallization and impedes water evaporation.

To overcome this challenge, we implemented a flipping strategy for the device. After ≈30 min of operation, we periodically flipped the device with the positive termination of the voltage meter always connected to the top electrode. The voltage initially decreased to 0.1 V and then gradually increased to its maximum value (0.278 V) under solar irradiation. This flipping process also allowed the electrode material to recharge and continue generating electricity in subsequent cycles, in mimic to the discharge/charge process of a rechargeable battery. Therefore, the device was able to stably generate electricity and fresh water for more than 240 h at a solar density of 1.0 kW m^{-2} (Figure 3g).

It's important to note that sodium ions in water undergo a solvation process where individual water molecules surround the sodium ion, forming a hydrated sodium ion complex. And the presence of coordinated water molecules can help reduce the electrostatic repulsion between these sodium and the host materials.[31] That is to say, the layered structure and extended interlayer spacing provide sufficient space for the storage of guest ions surrounded by hydrated water molecules. Therefore, the extended interlayer spacing of PANI@GO/MnO_2 in our device played a crucial role in facilitating the storage of sodion. The coordinated water molecules can stabilize the sodium within the interlayer regions of the PANI@GO/MnO_2, mitigating the electrostatic repulsion and promoting a more stable structure. Similar performance with large interlayer spacing has been observed in the layered structure-based materials.[32,33] Additionally, we compared the performance of our device with other reported devices for harvesting salinity-gradient energy in Figure 3h. The comparison includes power density and the ratio of measured V_{oc} to the theoretical value (V_T) predicted based on the sanity gradient (Table S1, Supporting Information). Our device demonstrates superior performance in both power density and V_{oc}/V_T. This superior performance of our device can be attributable to the PANI-reinforced layered structure with expanded interlayer spacing for PANI@GO/MnO_2 in the electrodes, which effectively restrain the collapse of the layered structure even when the device is periodically flipped, allowing stable operation in a wide range of NaCl concentrations (0.2–6.0 mol L^{-1}).

To investigate the factors contributing to the high V_{oc} of our device, we conducted a series of controlled experiments (**Figure 4a**). The V_{oc} of the device was measured in the absence or presence of PANI@GO/MnO_2 electrodes, which was separated by a cation exchange membrane (CEM), an AEM, or a separator

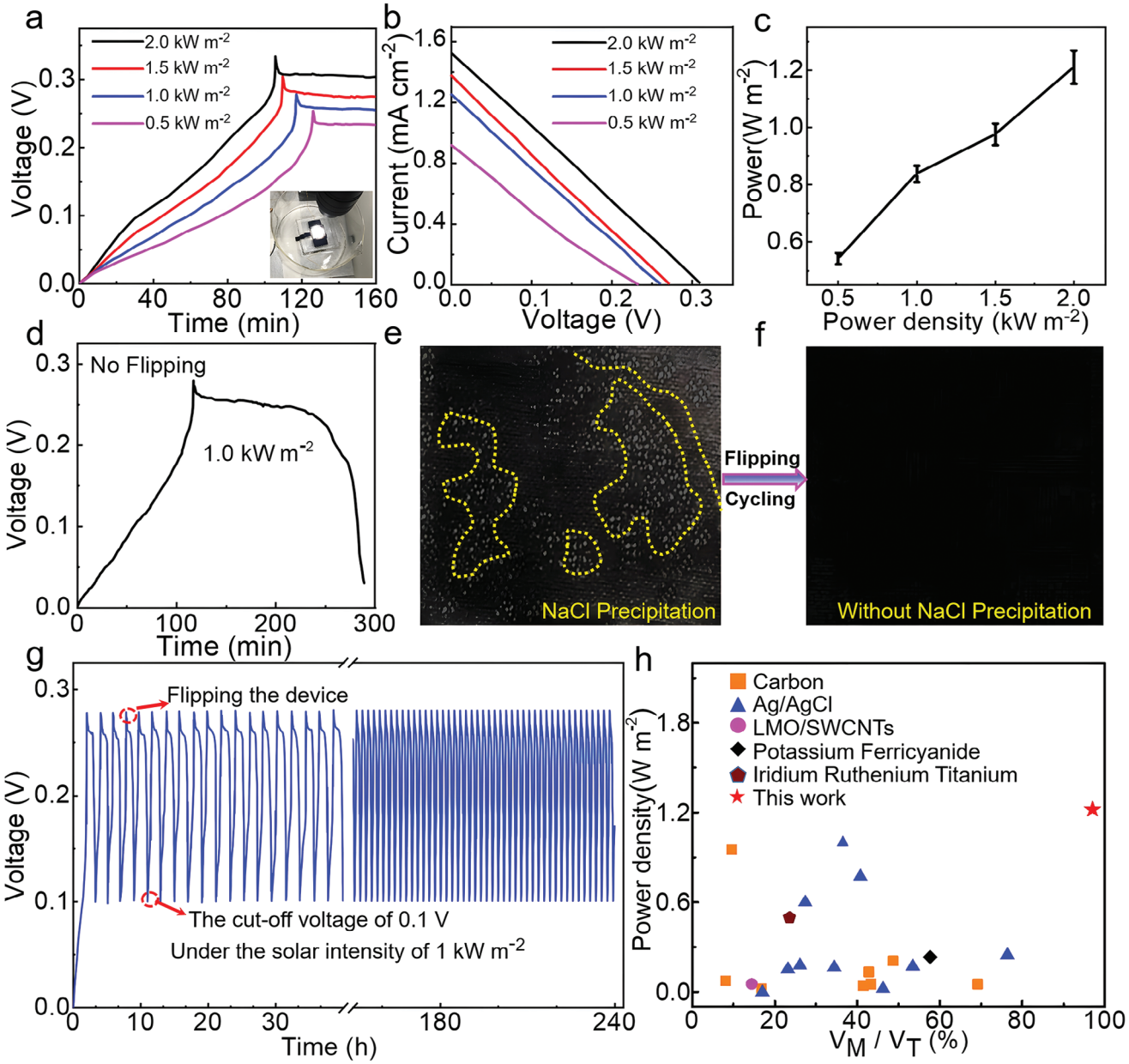

Figure 3. Salinity-gradient energy harvested from the evaporation under solar irradiation. a) The V_{oc} of the device over time under different solar irradiations, the inset is the photograph of integrated device under solar irradiation. b) The characteristic current-voltage curves of integrated device under different solar irradiations. c) The output power of the device under different solar irradiations. d) The V_{oc} of device over time under solar intensity of 1 kW m^{-2} without flipping. e,f) Photographs of solar absorbers from the integrated device without flipping at the 1st cycle (e) and with flipping at the 121st cycle (f). g) The V_{oc} of the device recorded for 121 cycles by periodically flipping the device (under the solar intensity of 1 kW m^{-2}). (h) Power density and measured voltage/ theoretical voltage (V_M/ V_T) reported previously, in comparison with our results, referring to Table S1 (Supporting Information), for details.

(limited selection on the ions) under illumination of 2.0 kW m^{-2} (Figure 4b). When the device contained two carbon cloth electrodes and a separator operated in NaCl or KCl solution, the V_{oc} was only ≈0.040 V, manifesting the small junction potential developed across the separator (Figure S14, Supporting Information). It seems likely that the separator can assist the transportation of chloridion selectively and resulted in a small membrane potential. When the device contained two PANI@GO/MnO_2 electrodes and a separator, the V_{oc} was 0.202 V, which was attributed to the intercalating redox reaction with sodion on the surface of PANI@GO/MnO_2 electrodes. The obtained V_{oc} (0.202) was slightly higher than the theoretical value (0.169 V) due to the potential developed across the separator.

When the device contained two carbon cloth electrodes and an AEM, the measured V_{oc} was 0.150 V, due to the selective chloridion transportation from the top to the bottom of the AEM. There

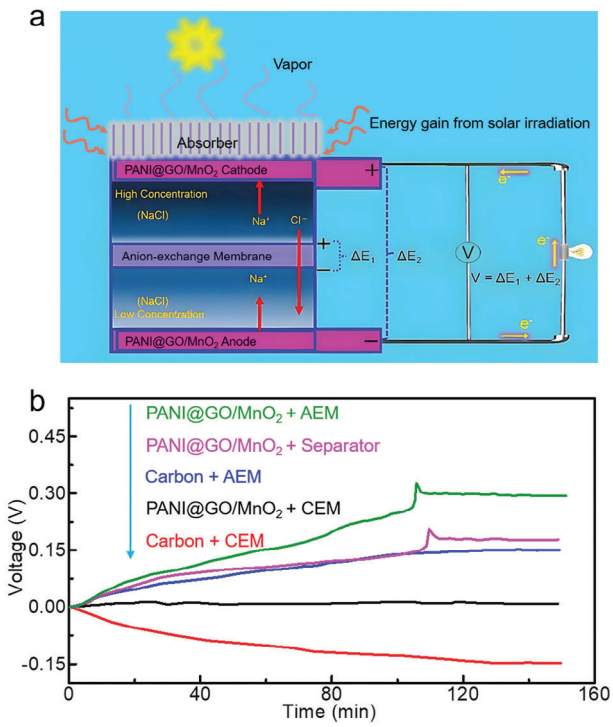

Figure 4. The potentials developed at the electrode and across the separator from the salinity-gradient under illumination. a) The schematic of the device describing the potentials developed from the electrode and the membrane. b) The V_{oc} obtained by using PANI@GO/MnO_2 electrode and carbon cloth electrode with different membranes under illumination of 2.0 kW m^{-2}.

is a difference between the measured value (0.150 V) and theoretical value (0.169 V), the possible reason was that the AEM does not have perfect selectivity, which reduced the membrane potential. When the device contained two PANI@GO/MnO_2 electrodes and an AEM, the measured V_{oc} was 0 .325 V. In our investigations, we observed that when PANI@GO/MnO_2 electrodes were combined with a CEM, the measured V_{oc} was nearly 0 V. On the other hand, when two carbon cloth electrodes were separated by a CEM, the obtained V_{oc} was −0.147 V. This indicates that the positive V_{oc} generated by the PANI@GO/MnO_2 electrodes and the negative V_{oc} produced by the CEM balanced each other out in this configuration. With these results from the above analyses, it can be confirmed that the high V_{oc} is attributed to the redox reaction of PANI@GO/MnO_2 electrodes and potential developed across the AEM due to selective transportation of chloridion.

To further understand the redox reaction of PANI@GO/MnO_2 electrode during the electricity generation, various characterization techniques were applied to examine the PANI@GO/MnO_2 electrode at different states (**Figure 5**). For the pristine PANI@GO/MnO_2 electrode (Figure 5a,b), there was no distinct change, but for the discharge state (after 1 cycle), increasingly large flakes formed during discharging (Figure 5c,d; Figure S15a,b, Supporting Information). Furthermore, TEM and HR-TEM images (Figure S15c,d, Supporting Information) of the PANI@GO/MnO_2 at the discharge state after 100 cycles closely resembled those of the discharge state after 1 cycle. Besides, the obtained SEM and TEM of the PANI@GO/MnO_2 at the charge state was almost the same as the pristine state after 100 cycles (Figure S16, Supporting Information). And the high-resolution transmission electron microscopy (HR-TEM) image was characterized (Figure S15, Supporting Information), and lattice spacings exhibited interplanar spacings of 0.24 and 0.27 nm, corresponding to the (201) and (350) planes of the $Na_{0.44}MnO_2$ crystalline, which were consistent with the XRD characterization (Figure S17, Supporting Information). Compared with the transmission electron microscopy and energy dispersive spectroscopy (TEM-EDS) mappings for PANI@GO/MnO_2 electrode at the pristine state (Figure 5b_1–b_4), the Na and Mn elements were homogeneous distribution at the discharge state (Figure 5d_1–d_4). Additionally, the oxidation state and atomic environment of Mn at different states had been studied (Figure 5e–g). Two asymmetric peaks of Mn 2p with the binding energies of 642.3 and 653.7 eV can be observed for the pristine PANI@GO/MnO_2, indicating the presence of Mn^{4+} (Figure 5e).[34–36] In contrast, the binding energy shifted to a lower value, indicating a decreased oxidation state of Mn in the compound at the discharge state after 1 cycle. As shown in Figure 5f, both peaks located at 642.8 and 654.3 eV were assigned to the Mn^{4+},[37] while another two peaks situated at 641.9 and 653.1 eV were due to Mn^{3+}. The presence of Mn^{4+} along with Mn^{3+} manifested that the Mn^{4+} were reduced from the pristine state to the discharge state.[34] Upon charging at the 100th cycle, oxidation state of Mn in the electrode almost came back to its pristine state (Figure 5g). Ex situ XPS spectra, particularly the survey spectrum of the PANI@GO/MnO_2 electrode at various states (Figure S18, Supporting Information), confirm the spectra's close resemblance to the original even at the charge state after 100 cycles. The additional peak of Na 1s in the discharge state spectrum indicates the formation of $Na_{0.44}MnO_2$. Furthermore, the XRD patterns of PANI@GO/MnO_2 exhibit excellent maintenance after 100 cycles (Figure S19, Supporting Information), suggesting the structural integrity of the electrode. These results showcase a robust and reversible reaction within the PANI@GO/MnO_2 electrode, characterized by a large interlayer distance. The electrode effectively accommodates the insertion and extraction of sodion within the wide concentration range of 0.2–6.0 mol L^{-1} during the cyclic operation of the integrated device, facilitated by the periodic flipping strategy.

It is important to assess the energy flux in the integrated system. The schematic of the energy flux of the device was shown in Figure 6a. The total energy input is derived from solar irradiation, which is then converted into thermal energy by the solar absorber. The generated hot vapor carries away most of the heat energy, while the remaining heat is dissipated through thermal irradiation, conduction, and convection. The solar absorber with high temperature promoted fast water evaporation, generating significant salinity difference between the two sides of the AEM. This salinity-gradient energy is then converted into electrical power through the PANI@GO/MnO_2 electrode.

The conversion efficiencies of solar energy to salinity power were from ≈1.1% to ≈2.5% under different solar irradiations (from 0.5 to 2.0 kW m^{-2}), as shown in Figure 6b. The theoretical salinity power was ≈17.62 W m^{-2} at the solar density of 1.0 kW m^{-2}, which increased to 50.2 W m^{-2} at the solar density of 2.0 kW m^{-2}. The efficiency of salinity power to electricity output was also calculated (Figure 6b), which was from ≈2.4% to ≈10.1% under

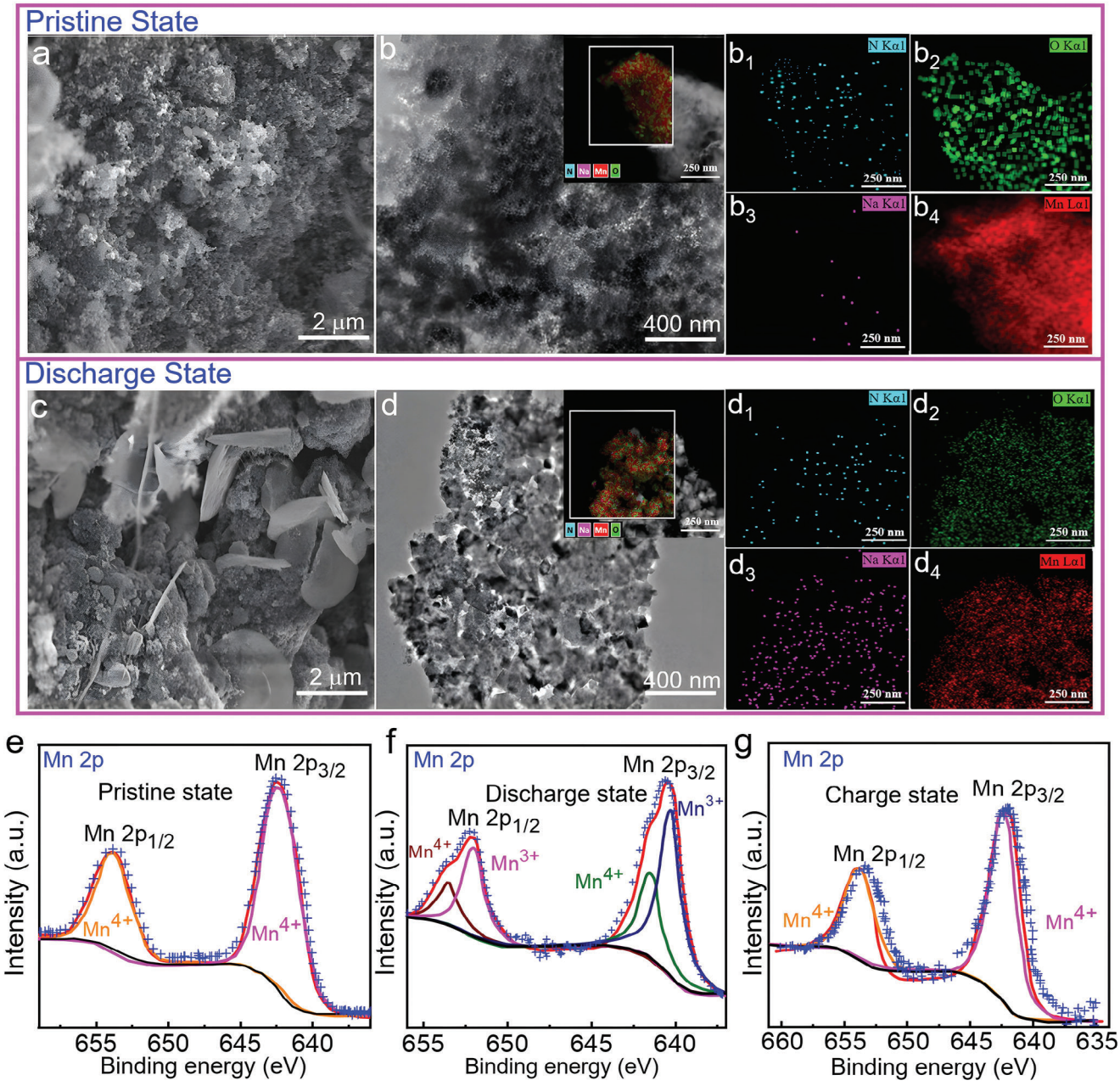

Figure 5. Structure characterizations of the PANI@GO/MnO_2 electrodes. a) Typical SEM image and TEM image b) of pristine PANI@GO/MnO_2. (b_1-b_4) TEM-EDS elemental mappings for nitrogen (b_1), oxygen (b_2), sodium (b_3), manganese (b_4) of the pristine PANI@GO/MnO_2. c,d) SEM image (c) and TEM image (d) of PANI@GO/MnO_2 after discharge at the 1st cycle. (d_1-d_4) TEM-EDS elemental mappings for nitrogen (d_1), oxygen (d_2), sodium (d_3), manganese (d_4) of PANI@GO/MnO_2 after discharge at the 1st cycle. (e-g) XPS narrow scan spectra for PANI@GO/MnO_2 at pristine state e), discharge state f) at the 1st cycle, and charge state g) at the 100th cycle.

the different solar intensities (from 0.5 to 2.0 kW m^{-2}). The efficiency of our device is higher than the reported membrane-based devices.[38]

The proof-of-concept prototype (with large scale) and series connections of the devices were built to demonstrate the feasibility of the design for practical applications (Figure 6). The active area of the single device was extended to 100 cm^2 (with size of ≈10 cm × 10 cm), a I_{sc} of 72.5 mA and a V_{oc} of 0.31 V were obtained at the solar density of 1.0 kW m^{-2}, which could produce a maximum power of 5.6 mW (Figure 6c; Figures S20 and S21, Supporting Information). Figures S22 and S23 (Supporting Information) show the different series connections of the devices and their electricity generation performance. When eight devices (with size of ≈5 cm × 5 cm, V_{oc} of 0.28–0.31 V and I_{sc} of 27.5–28.7 mA) were connected in series, the V_{oc} was scaled up to ≈2.38 V (Figure 6d,g), which could power the designed fan with the LED lights signal for the abbreviation of Tsinghua University (THU) and Nanjing University of Aeronautics and

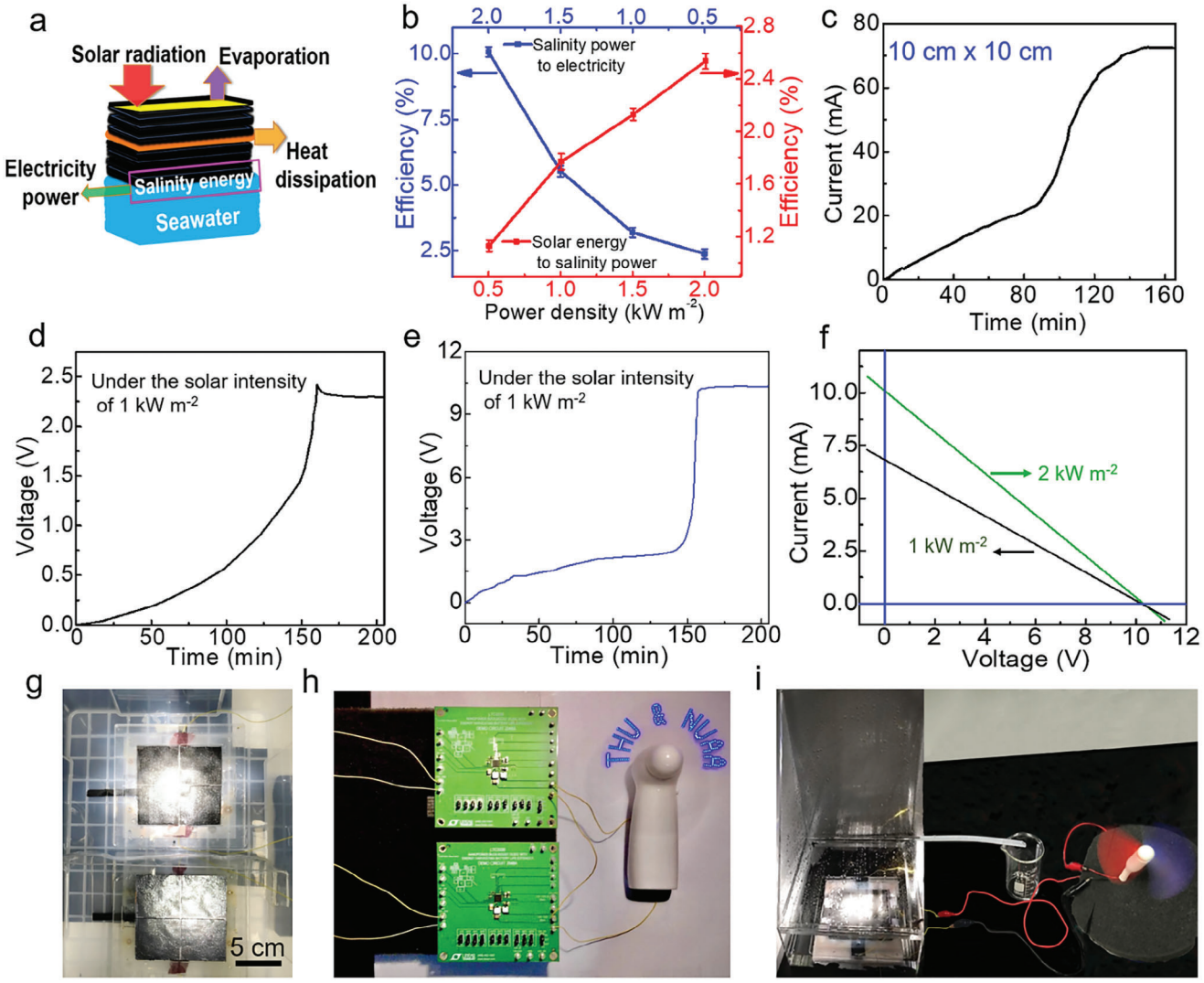

Figure 6. Energy-transfer efficiency analysis and scaling applications of the integrated system prototype. a) Schematic diagram of energy flux and the efficiency of the integrated device. b) The conversion efficiencies of solar energy to salinity power and salinity energy to output electricity under the different solar intensities. c) I_{sc} of the integrated device with an area of 100 cm^2 under illumination of 1.0 kW m^{-2}. d) The V_{oc} of eight individual devices (≈5 cm × 5 cm) connected in series. e) The V_{oc} of the device in **Figure 6**d after connecting a source-free boost converter (DC 2048A) in the circuit. f) The current–voltage curve of the integrated device in Figure 6d under the solar intensity of 1 and 2 kW m^{-2} after connecting the boost converter. g) Photograph of the integrated device. h) The photograph of the designed fan with dynamic LED powered by eight devices (with size of ≈5 cm × 5 cm) connected in series with the boost converter in the circuit under the solar intensity of 1 kW m^{-2}. i) The simultaneous generation of clean water and electricity from the device. As shown in the Figure 6h, the content of the LED light signal is the abbreviation of Tsinghua University (THU) and Nanjing University of Aeronautics and Astronautics (NUAA).

Astronautics (NUAA) through boosting the output voltage to 10 V by using two source-free boost converters (DC 2048A, Figure 6h). The V_{oc} and the current-voltage curves of the devices after connecting source-free boost converters in the circuit are shown in Figure 6e and Figure 6f. The photographs of the corresponding integrated device and the source-free boost converter can be seen in Figure S24a,b (Supporting Information), respectively. In addition to electricity generation, our integrated device facilitated the production of clean water through condensation of the steam generated by water evaporation (Figure 6i). To assess the desalination performance, the concentrations of metal ions (Na^+, Ca^{2+}, Mg^{2+}, Pb^{2+}) in the obtained clean water were measured and shown in Figure S25 (Supporting Information), the ion concentrations were found to be below the drinking water standards set by the World Health Organization (WHO) in comparison to synthetic seawater.[39,40] This demonstrates the efficient desalination capability of our device. To further demonstrate the universality of the integrated system as a self-sustaining energy device, an integrated device with a volume of one cubic meter is designed (see Figure S26, Supporting Information). The amplified assembly system can function as a self-sustaining energy device through the synergistic processes of water evaporation cooling, power generation, and water purification.

3. Conclusion

This work demonstrates a significant advancement in the field of simultaneous clean water and electricity generation through solar evaporation. The output voltage is significantly improved by combining the membrane potentials and the battery electrode in the integrated electrochemical system. The experimental results showed that the integrated device can generate electricity (≈1.1 W m^{-2}) and producing clean water (1.25 kg m^{-2} h^{-1}) simultaneously from synthetic seawater under one sun irradiation, and the energy-transfer efficiency of salinity energy to electricity reaches 5.5% via 78.9% solar energy. It is noted that the symmetrical electrodes with PANI@GO/MnO_2 can work steadily with high reversibility in the quite large NaCl concentration range by periodically flipping the integrated device. With further optimization and efficient design strategies, it is possible to improve the electricity output properties and solar desalination performance of the integrated device. By utilizing low-cost electrodes, ensuring long-term cycling stability, and achieving high energy-transfer efficiency, this technique presents a promising solution for harvesting blue energy. Such a solution is particularly valuable for off-grid remote areas where access to clean water and electricity is critical.

4. Experimental Section

Materials and Reagents: $KMnO_4$, Aniline, CCl_4, and $(NH_4)_2S_2O_8$ were purchased from Sigma Aldrich (Inc. St. Louis, MO.USA). NaCl, KCl, HNO_3, H_2SO_4, hydrochloric acid, carbon cloth, Graphite particles, MWCNTS, carbon black and polytetrafluoroethylene were obtained from Sinopharm Chemical Reagent Co. Ltd. AEM was obtained from Versogen, CEM was provided by Chemours Co. Ltd.

Fabrication of PANI@GO/MnO_2: The PANI anchored GO intercalated layered MnO_2 nanocomposite was synthesized via inorganic/organic interfacial reaction. In a typical synthesis process, graphite oxide (0.19 g), first prepared by the modified Hummers' method was dispersed into 375 mL of de-ionized water. Then, 0.35 g of pristine $KMnO_4$ was added into the solution, which was kept in an ultra-sonication (250 W, 220 V) and maintained at 40 kHz for 45 min to obtain a homogeneous mixture. Aniline (7 mL) was dissolved in 400 mL CCl_4. The solution containing aniline was added into the homogeneous mixture. At a constant stirring rate, the above two solutions were mixed in an ice-water bath, showing an aqueous/organic stratification system in the reaction vessel. After 20 min, a mixture of hydrochloric acid (2.75 M), $(NH_4)_2S_2O_8$ in de-ionized water (25 mL) was slowly added to the reactor under stirring for another 20 min. Subsequently, reaction system was kept in the ice-water bath for 24 h. The product was finally obtained by using centrifugal separation, along with washing several times in ethanol and de-ionized water. The resultant material was vacuum-dried at 45 °C for 24 h. The molar ratio of aniline and $(NH_4)_2S_2O_8$ in the reaction system was 1:1. All chemicals were of analytical grade and used as-received.

Fabrication of solar Absorbers Coated on the Carbon Cloth: A piece of carbon cloth with a designed profile except the electrode tab was soaked in concentrated HNO_3 for 4.5 hr. After the oxidation reaction, the carbon cloth was washed with DI water and alcohol to remove the residual acid, then it was dried at 75 °C in a vacuum oven for 12 hr. Graphite particles (the particle diameter was ≈20 nm) were dispersed in water followed by 3 h of ultrasonication, the concentration of which was 10 mg mL^{-1}. MWCNTS (4 g) were dispersed in the 150 mL mixed acid solutions (H_2SO_4/HNO_3 = 3/1, v/v) followed by 0.5 h of ultrasonication, then the mixture was transferred to a refluxing device in the 95 °C oil bath for 2.5 h with vigorously stirring. After the system was cooled at room temperature, the extracted MWCNTS were washed with DI water several times until the supernatant was neutral. The pre-acidized MWCNTs were redispersed in DI water to form MWCNTs ink (the concentration was 10 mg mL^{-1}). The Graphite solution (25 mL) and MWCNTs ink (50 mL) were simultaneously added dropwise to a flask, followed by 7 h of vigorous stirring and 1 h of sonication to form a homogeneous solar absorbers suspension. The obtained solar absorbers suspension was dropcasted on the pre-treated carbon cloth and dried at 80 °C in a vacuum oven overnight.

Fabrication of Electrode: The electrode was composed of a solar absorbers layer, a current collector, and an electrode material layer. Composite electrode slurry was fabricated by mixing PANI@GO/MnO_2 (80 wt %), carbon black (10 wt %) and polytetrafluoroethylene (10 wt %) with water. In the former case, pre-treated carbon cloth with graphite particles and SWCNTs fabricated by drop-casting method were used as solar absorbers, and the obtained homogeneous electrode material slurry layer was attached to the other side of carbon cloth by the pressing method (≈3 MPa) in a hot-pressing apparatus, followed by drying under vacuum at 80 °C for 24 hr. The corresponding mass of PANI@GO/MnO_2 on electrode material layer was ≈5.0 mg cm^{-2}. Eventually, the effective areas of electrodes were controlled at 1 cm^2 (1 cm × 1 cm), 9 cm^2 (3 cm × 3 cm), 25 cm^2 (5 cm × 5 cm) and 100 cm^2 (10 cm × 10 cm), respectively.

Fabrication of Integrated Device: This integrated device combined solar desalination and electricity generation under simulated sunlight as shown in Figure 1a and Figure 1b. The device contained two symmetrical electrodes separated by an anion-exchange membrane (100 µm), which were integrated by the molded organic glasses (thickness 0.4 cm) and shaped gaskets (thickness 0.5 mm). Additionally, the current collector in the electrode was cut into a designed area with two tails, which were the electrode tab (1.0 cm × 3.5 cm) and the water transportation belt (0.3 cm × 2 cm). The joints of each component in the device were sealed by using polydimethylsiloxane (PDMS, A/B = 10/1, v/v).

Energy Harvesting Experiments: To test the energy harvesting performance of the integrated system, 0.2 M NaCl solution (representative of seawater) and 0.2 M KCl solution were prepared. The I_{sc} and the V_{oc} of the device were measured by Keithley DMM6500. The electrical measurements for the device were performed with an electrochemical workstation (VMP3, Bio-Logic). The current-voltage curves of the integrated device were conducted at a scan rate of 50 mV s^{-1}. The maximum output of the device could be calculated by using the formula ($P_{max} = V_{oc} I_{sc} / 4$). The integrated device cycled by flipping the symmetrical electrodes vertically 180 degrees (from top to bottom), when the voltage of the device was decreasing below 100 mV (cutoff voltage).

Characterization: The pore size distribution and specific surface area of the samples were calculated by the Brunauer—Emmett–Teller (BET) and Barrett–Joyner–Halenda (BJH) models from N_2 adsorption isotherms at 77 K (ASAP 2020M+C). Thermogravimetric (TG) analysis was implemented to ascertain the changes in the weight of the samples with increasing temperature (DSC3). Raman spectroscopy measurements of samples were obtained using a Horiba LabRAM HR800 confocal Raman microscope system. The presence of different modes of vibrations of samples was investigated using a Fourier transform infrared spectrophotometer (FTIR, Nicolet is 50) over the range from 400 to 3600 cm^{-1} with a resolution of 2 cm^{-1}. The light absorption of solar absorbers was performed via UV—Vis–NIR Spectrophotometer (Cary 5000), the Cary is equipped with an integrating sphere, the reflection and transmission measurements of this instrument cover a spectral range from 250 nm to 2500 nm. X-ray diffraction (XRD) data was obtained on a Bruker DS RINT2000/PC diffractometer with a Cu-Kα1 source (λ = 1.5418 Å) to research the crystal structure of samples. Scanning electron microscopy (SEM) was conducted on a field-emission scanning electron microscopy (HITACHI SU8010). The detailed microstructure of samples was characterized by a transmission electron microscopy (TEM) with an accelerating voltage of 200 kV (JEM 2100F). X-ray photoelectron spectroscopy (XPS) measurements were carried out with an XPS spectrometer (ESCALABSB 250 Xi) for detecting the surface element composition and the bonding configuration of samples. The solar light was provided by a solar simulator (Newport and Perfect Light), which can supply different light intensity according to collecting lens. The mass change of solar steam generation from the system was obtained using high accuracy balance (Mettler-Toledo, ME104E). The

thermal diffusion coefficient of the AEM was measured by a laser flash apparatus (NETZSCH, LFA447), and the heat capacity was measured by a differential scanning calorimeter (Mettler Toledo, DSC 3).

Acknowledgements

This work was supported by the National Key Research and Development Project (No.2019YFA0705403), the National Natural Science Foundation of China (No. T2293691; 52102276; T2293693; 12150002; 12172176), the Guangdong Innovative and Entrepreneurial Research Team Program (No. 2017ZT07C341), the Guangdong Basic and Applied Basic Research Foundation (No. 2020B0301030002), and the Shenzhen Basic Research Project (Nos. WDZC20200824091903001, JSGG20220831105402004, JCYJ20190809180605522).

Conflict of Interest

The authors declare no conflict of interest.

Data Availability Statement

The data that support the findings of this study are available in the supplementary material of this article.

Keywords

anion-exchange membrane, electrochemical potentials, high-efficiency device, salinity concentration gradient, solar steam generation

[1] Z. Zhang, X. Li, J. Yin, Y. Xu, W. Fei, M. Xue, Q. Wang, J. Zhou, W. Guo, *Nat. Nanotechnol.* **2018**, *13*, 1109.
[2] A. S. Arico, P. Bruce, B. Scrosati, J. M. Tarascon, *Nat. Mater.* **2005**, *4*, 366.
[3] B. E. Logan, K. Rabaey, *Science* **2017**, *337*, 686.
[4] J. Schewe, J. Heinke, D. Gerten, I. Haddeland, N. W. Arnell, D. B. Clark, R. Dankers, S. Eisner, B. M. Fekete, F. J. Colon-Gonzalez, S. N. Gosling, H. Kim, X. Liu, Y. Masaki, F. T. Portmann, Y. Satoh, T. Stacke, Q. Tang, Y. Wada, D. Wisser, T. Albrecht, K. Frieler, F. Piontek, L. Warszawski, P. Kabat, *Proc. Natl. Acad. Sci* **2014**, *111*, 3245.
[5] M. M. Mekonnen, A. Y. Hoekstra, *Sci. Adv.* **2016**, *2*, 1500323.
[6] A. Siria, M. L. Bocquet, L. Bocquet, *Nat. Rev. Chem.* **2017**, *1*, 0091.
[7] J. Feng, M. Graf, K. Liu, D. Ovchinnikov, D. Dumcenco, M. Heiranian, V. Nandigana, N. R. Aluru, A. Kis, A. Radenovic, *Nature* **2016**, *536*, 197.
[8] D. Brogioli, *Phys. Rev. Lett.* **2009**, *103*, 058501.
[9] A. Cipollina, M. Giorgio, *Sustainable Energy From Salinity Gradients*, Woodhead Publishing, Cambridge, UK **2016**.
[10] A. P. Straub, A. Deshmukh, M. Elimelech, *Energy Environ. Sci.* **2016**, *9*, 31.
[11] G. Z. Ramon, B. J. Feinberg, E. M. Hoek, *Energy Environ. Sci.* **2011**, *4*, 4423.
[12] B. E. Logan, M. Elimelech, *Nature* **2012**, *488*, 313.
[13] N. Y. Yip, A. Tiraferri, W. A. Phillip, J. D. Schiffman, L. A. Hoover, Y. C. Kim, M. Elimelech, *Environ. Sci. Technol.* **2011**, *45*, 4360.
[14] E. Bar-Zeev, F. Perreault, A. P. Straub, M. Elimelech, *Environ. Sci. Technol.* **2015**, *49*, 13050.
[15] N. Y. Yip, D. Brogioli, H. V. Hamelers, K. Nijmeijer, *Environ. Sci. Technol.* **2016**, *50*, 12072.
[16] R. E. Pattle, *Nature* **1954**, *174*, 660.
[17] J. N. Weinstein, F. B. Leitz, *Science* **1976**, *191*, 557.
[18] P. Yang, K. Liu, Q. Chen, J. Li, J. Duan, G. Xue, Z. Xu, W. Xie, J. Zhou, *Energy Environ. Sci.* **2017**, *10*, 1923.
[19] L. Wu, Z. Dong, Z. Cai, T. Ganapathy, N. X. Fang, C. Li, C. Yu, Y. Zhang, Y. Song, *Nat. Commun.* **2020**, *11*, 521.
[20] X. Li, W. Xu, M. Tang, L. Zhou, B. Zhu, S. Zhu, J. Zhu, *Proc. Natl Acad. Sci* **2016**, *113*, 13953.
[21] M. Elimelech, W. A. Phillip, *Science* **2011**, *333*, 712.
[22] X. Li, X. Min, J. Li, N. Xu, P. Zhu, B. Zhu, S. Zhu, J. Zhu, *Joule* **2018**, *2*, 2477.
[23] P. Tao, G. Ni, C. Song, W. Shang, J. Wu, J. Zhu, T. Deng, *Nat. Energy* **2018**, *3*, 1031.
[24] J. W. Post, J. Veerman, H. V. M. Hamelers, G. J. W. Euverink, S. J. Metz, K. Nymeijer, C. J. N. Buisman, *J. Membr. Sci.* **2007**, *288*, 218.
[25] Y. Fu, Q. Wei, G. Zhang, X. Wang, J. Zhang, Y. Hu, D. Wang, L. Zuin, T. Zhou, Y. Wu, S. Sun, *Adv. Energy Mater.* **2018**, *8*, 1801445.
[26] H. Ghasemi, G. Ni, A. M. Marconnet, J. Loomis, S. Yerci, N. Miljkovic, G. Chen, *Nat. Commun.* **2014**, *5*, 4449.
[27] L. Zhou, Y. Tan, D. Ji, B. Zhu, P. Zhang, J. Xu, Q. Gan, Z. Yu, J. Zhu, *Sci. Adv.* **2016**, *4*, 150122.
[28] K. Bae, G. Kang, S. K. Cho, W. Park, K. Kim, W. J. Padilla, *Nat. Commun.* **2015**, *6*, 10103.
[29] Y. Ito, Y. Tanabe, J. Han, T. Fujita, K. Tanigaki, M. Chen, *Adv. Mater.* **2015**, *27*, 4302.
[30] B. S. Joo, I. S. Kim, I. K. Han, H. Ko, J. G. Kang, G. Kang, *Appl. Surf. Sci.* **2022**, *583*, 152563.
[31] Y. Li, S. Zhu, Z. Liu, *J. Am. Chem. Soc.* **2016**, *138*, 5371.
[32] D. Kundu, B. D. Adams, V. Duffort, S. H. Vajargah, L. F. Nazar, *Nat. Energy* **2016**, *1*, 16119.
[33] B. Dunn, H. Kamath, J. M. Tarascon, *Science* **2011**, *334*, 928.
[34] M. Toupin, B. Thierry, B. Daniel, *Chem. Mater.* **2004**, *16*, 3184.
[35] Y. Li, J. Xu, T. Feng, Q. Yao, J. Xie, H. Xie, *Adv. Funct. Mater.* **2017**, *27*, 1606728.
[36] J. Long, J. Gu, Z. Yang, J. Mao, J. Hao, Z. Chen, Z. Guo, *J. Mater. Chem. A* **2019**, *7*, 17854.
[37] J. Long, F. H. Yang, J. Cuan, J. Wu, Z. Yang, H. Jiang, R. Song, W. Song, J. Mao, Z. Guo, *ACS Appl. Mater. Interfaces* **2020**, *12*, 32526.
[38] J. Gao, W. Guo, D. Feng, H. Wang, D. Zhao, L. Jiang, *J. Am. Chem. Soc.* **2014**, *136*, 12265.
[39] F. Edition, *WHO Chron.* **2011**, *38*, 104.
[40] S. P. Surwade, S. N. Smirnov, I. V. Vlassiouk, R. R. Unocic, G. M. Veith, S. Dai, S. M. Mahurin, *Nat. Nanotech.* **2015**, *10*, 459.